



HAL
open science

Impact of Surface Soil Moisture Variations on Radar Altimetry Echoes at Ku and Ka Bands in Semi-Arid Areas

Christophe Fatras, Pierre Borderies, Frédéric Frappart, Éric Mougin, Denis Blumstein, Fernando Nino

► **To cite this version:**

Christophe Fatras, Pierre Borderies, Frédéric Frappart, Éric Mougin, Denis Blumstein, et al.. Impact of Surface Soil Moisture Variations on Radar Altimetry Echoes at Ku and Ka Bands in Semi-Arid Areas. *Remote Sensing*, 2018, 10 (4), 182, p. 1-23. 10.3390/rs10040582 . hal-02315123

HAL Id: hal-02315123

<https://hal.science/hal-02315123>




Submitted on 14 Oct 2019

HAL is a multi-disciplinary open access archive for the deposit and dissemination of scientific research documents, whether they are published or not. The documents may come from teaching and research institutions in France or abroad, or from public or private research centers.

L'archive ouverte pluridisciplinaire **HAL**, est destinée au dépôt et à la diffusion de documents scientifiques de niveau recherche, publiés ou non, émanant des établissements d'enseignement et de recherche français ou étrangers, des laboratoires publics ou privés.

Article

Impact of Surface Soil Moisture Variations on Radar Altimetry Echoes at Ku and Ka Bands in Semi-Arid Areas

Christophe Fatras ^{1,2,*} , Pierre Borderies ¹, Frédéric Frappart ^{2,3}, Eric Mougin ² , Denis Blumstein ^{3,4} and Fernando Niño ³ 

¹ Office National d'Etudes et de Recherches Aérospatiales (ONERA), 2 Avenue Edouard Belin, 31055 Toulouse CEDEX 4, France; pierre.borderies@onera.fr

² Geosciences Environnement Toulouse (GET), UMR 5563, CNRS/IRD/UPS, Observatoire Midi-Pyrénées 8 (OMP), 14 Avenue Edouard Belin, 31400 Toulouse, France; frederic.frappart@legos.obs-mip.fr (F.F.); eric.mougin@get.omp.eu (E.M.)

³ Laboratoire d'Etudes en Géophysique et Oceanographie Spatiales (LEGOS), UMR 5566, CNRS/IRD/UPS, Observatoire Midi-Pyrénées 8 (OMP), 14 Avenue Edouard Belin, 31400 Toulouse, France; denis.blumstein@cnes.fr (D.B.); fernando.nino@ird.fr (F.N.)

⁴ Centre National d'Etudes Spatiales (CNES), 18 Avenue Edouard Belin, 31400 Toulouse, France

* Correspondence: christophe.fatras@gmail.com; Tel.: +33-561-332-970

Received: 28 February 2018; Accepted: 3 April 2018; Published: 9 April 2018



Abstract: Radar altimetry provides information on the topography of the Earth surface. It is commonly used for the monitoring not only sea surface height but also ice sheets topography and inland water levels. The radar altimetry backscattering coefficient, which depends on surface roughness and water content, can be related to surface properties such as surface soil moisture content. In this study, the influence of surface soil moisture on the radar altimetry echo and backscattering coefficient is analyzed over semi-arid areas. A semi-empirical model of the soil's complex dielectric permittivity that takes into account that small-scale roughness and large-scale topography was developed to simulate the radar echoes. It was validated using waveforms acquired at Ku and Ka-bands by ENVISAT RA-2 and SARAL AltiKa respectively over several sites in Mali. Correlation coefficients ranging from 0.66 to 0.94 at Ku-band and from 0.27 to 0.96 at Ka-band were found. The increase in surface soil moisture from 0.02 to 0.4 (i.e., the typical range of variations in semi-arid areas) increase the backscattering from 10 to 15 dB between the core of the dry and the maximum of the rainy seasons.

Keywords: radar altimetry; waveform; dielectric permittivity; soil moisture

1. Introduction

The semi-arid region of West-Africa has been identified by [1] as a hot-spot for surface-atmosphere coupling, and where the routine monitoring of soil moisture would improve boreal summer seasonal forecasting. Moreover, the monitoring of the temporal variations of the surface soil moisture (SSM), i.e., the water content in the upper soil profile, is of primary importance in semi-arid regions, since SSM drives the evapotranspiration flux to the atmosphere via the partition between infiltration and run-off, and between soil evaporation and plant transpiration [2]. The surface soil moisture thus modulates the latent and sensible energy fluxes at the surface [3]. In semi-arid conditions, SSM also influences the main ecohydrological surface processes such as the plant germination, growth and mortality [4], the degradation and mineralization of the organic matter and the emission of gaseous compounds [5].

Accordingly, in semi-arid regions (i.e., in water limited systems), SSM is probably the main relevant Essential Climate Variable (ECV) that needs to be monitored at different temporal and spatial scales.

Spaceborne active microwave remote sensing offers different techniques and instruments to monitor SSM in semi-arid regions. Low spatial resolution systems between approximately 25 and 50 km, but with a high temporal resolution of a few days, such as the wind scatterometers onboard the European Remote Sensing (ERS) Satellites, QuickSCAT, and the Advanced SCATterometer, (ASCAT), on board METOP, and radiometers such as the advanced microwave scanning radiometer, AMSR-E and the salinity moisture and ocean salinity satellite, SMOS, have shown considerable potential for monitoring SSM over semi-arid regions [6–10].

Specifically, it was demonstrated with the wind-scatterometer on-board ERS-1&2 [6,11,12] that spaceborne scatterometers can be used for estimating SSM. Wind scatterometers derived-SSM products are now widely used in combination with microwave radiometers products [13–15]. At higher spatial resolutions, synthetic aperture radar (SAR) such as ERS-1 and -2 SARs and ASAR onboard ENVISAT, have also shown great potentialities for deriving SSM [16–19].

Following the study conducted in Australia by the authors of [20], who demonstrated the effects of soil moisture and soil roughness on the nadir C- and Ku-band backscattering coefficients, recent studies demonstrated the capabilities of spaceborne altimeters for estimating SSM in semi-arid regions such as in west-Africa [21–24] and in Australia [25]. Indeed, thanks to their nadir-looking capability, altimeters minimize the attenuation by the vegetation layer and a relationship can be directly found with the moisture content of the underlying soil. Over the Sahel region where the vegetation density is generally low, a very good linear correlation was found between the backscattering coefficient measured at Ku-band by the ENVISAT RA2 radar altimeter and SSM, with correlation values higher than those found with SAR data over the same sites [19,21]. However, the effects of the altimeter frequency and of soil roughness were not investigated. Moreover, the dynamic range of the backscattered coefficient must be known in order to be taken into consideration in the inversion procedure of SSM.

The present study aims to investigate how the spatio-temporal variations of SSM and soil roughness impact the radar altimetry echoes or waveforms at Ku- and Ka- bands over a semi-arid region. To this end, a physically-based model which takes into account the interaction between the incident wave and the surface was developed. This manuscript is organized as follows: the altimetry waveform model, named Continental waveform ALtimetry Model (CALM), is presented in Section 2. Then the dataset used for simulating the scenes and used for validating the model, as well as the study sites are described in Sections 3 and 4, respectively. Modeling results are confronted to real data acquired by the Ku-band ENVISAT and Ka-band AltiKa altimeters, over five contrasted sites in terms of landscape, relief, roughness and heterogeneity of the illuminated surface, including the presence of open waters. The performance of the model in terms of waveform generation is analyzed in Section 5 and the impact of SSM on the altimetry signal is eventually studied through a sensitivity analysis (Section 6).

2. Radar Altimetry Backscattering Modeling

To simulate the electromagnetic interaction between the wave emitted by the altimeter antenna and the illuminated soil, a two scale approach is used. The antenna footprint on the soil is sampled using triangular facets in order to be able to take into account any topography. Each facet is characterized by small scale roughness parameters and soil dielectric permittivity. The approach consists in vectorially summing the complex contributions of all the facets at the receiver. The vectorial contribution of each facet is computed assuming that the field distribution over the facet is the same as if it were infinite. Note that the large scale sampling may be adapted to a multi-scale one all the more easily as the computations are very fast.

The Kirchoff model was used to take into account the small-scale roughness. It is used to simulate the electromagnetic (EM) response of a rough surface taking into account rms height (hrms) and the correlation length of the local surface. The macroscopic scale integrates the effect of the surface

topography in the altimeter footprint (several to several tenths of km² depending on the wavelength of the EM wave) through the use of a Digital Elevation Model (DEM). Due to the roughness parameters used in this study, the Kirchoff model was preferred to other models at our wavelengths [26].

2.1. Simulation of the Surface Backscattering Using the Kirchoff Model

2.1.1. Kirchoff Model of the Stationary Phase

The Kirchoff model for the stationary phase, also known as Geometric Optics (GO) backscattering model, is based upon the tangent plane approximation. The surface is represented as a mosaic of randomly orientated planes, each one of them locally tangent to the surface. This model can be applied under the following assumptions:

$$kl > 6 \quad (1)$$

$$l^2 > 2.76s\lambda \quad (2)$$

$$kscos\theta > 1.5 \quad (3)$$

where $k = 2\pi/\lambda$ is the wavenumber and λ the wavelength, s the root mean square height (m) representing the surface roughness, l the surface correlation length (m), θ the wave incidence angle. s and l are the rms height and the correlation length.

In the GO model, each elementary surface has a proper backscattering coefficient (which is valid for VV and HH polarization) as expressed in the following equation:

$$\sigma_{HH}(\theta) = \sigma_{VV}(\theta) = \frac{\Gamma_0}{2m^2(\cos\theta)^4} \exp\left(-\frac{(\tan\theta)^2}{2m^2}\right) \quad (4)$$

where Γ_0 is the Fresnel reflection coefficient at nadir incidence and m the autocorrelation function that depends on the nature of the surface.

For a Gaussian surface, the autocorrelation function is:

$$m = \frac{\sqrt{2}s}{l} \quad (5)$$

For an exponential surface, the autocorrelation function is:

$$m = \frac{s}{l} \quad (6)$$

As Low Resolution Mode (LRM) altimeters are nadir-looking sensors, if the local slope is small, (3) becomes:

$$ks > 1.5 \quad (7)$$

The Fresnel coefficients at nadir incidence can be written as:

$$\Gamma_0 = \left| \frac{\sqrt{\varepsilon} - 1}{\sqrt{\varepsilon} + 1} \right|^2 \quad (8)$$

where ε is the soil dielectric permittivity.

2.1.2. Soil Dielectric Permittivity Estimates at Ku and Ka Bands

Soil dielectric permittivity estimates are determined using the semi-empirical from [27,28]. According to this model that extends earlier works from [29,30], the complex dielectric permittivity of a medium (ε_m) is defined as:

$$\varepsilon_m = \left(1 + \frac{\rho_b}{\rho_s}(\varepsilon_s^\alpha - 1) + m_v^\beta \varepsilon_{fw}^\alpha - m_v\right)^{\frac{1}{\alpha}} \quad (9)$$

where ε_s and ε_{fw} are the relative dry soil and effective free water permittivities respectively, ρ_b and ρ_s are the soil bulk and specific soil densities respectively, m_v is the volumetric soil moisture given in percent, α and β are the shape and empirical constants respectively. All details about the complex dielectric permittivity from [27,28] are given in Appendix A.

To our knowledge, no dielectric permittivity model has been specifically designed for the Ka-band. In this study, the semi-empirical model for soil complex dielectric permittivity, validated for the Ku-band was extended to the Ka-band as in previous studies [30,31].

2.2. Altimeter Waveform Generation

2.2.1. Vectorial Polarimetric Backscattering

The Forward Scattering Alignment convention (FSA) was chosen for all the computation at each elementary surface (see Appendix B for the description of the surface discretization), following the conventions detailed in [32]. To take into account the polarization, the emitted wave is considered to be linearly polarized with the electric field parallel to the X-axis (Figure A1).

Over a given triangular sample of barycenter O_i , the incident electromagnetic wave emitted by the altimeter (S for source in Figure 1) is directed along the wave vector \vec{k}_i , defined as:

$$\vec{k}_i = \frac{\vec{SO}_i}{|\vec{SO}_i|} \quad (10)$$

The components of the incident electric field \vec{E}_i following the three axes of the global vector set are defined by:

$$\vec{E}_i = \vec{k}_i \wedge \vec{y} = \begin{bmatrix} E_{Xi} \\ E_{Yi} \\ E_{Zi} \end{bmatrix} \quad (11)$$

where y is the norm vector in the y direction.

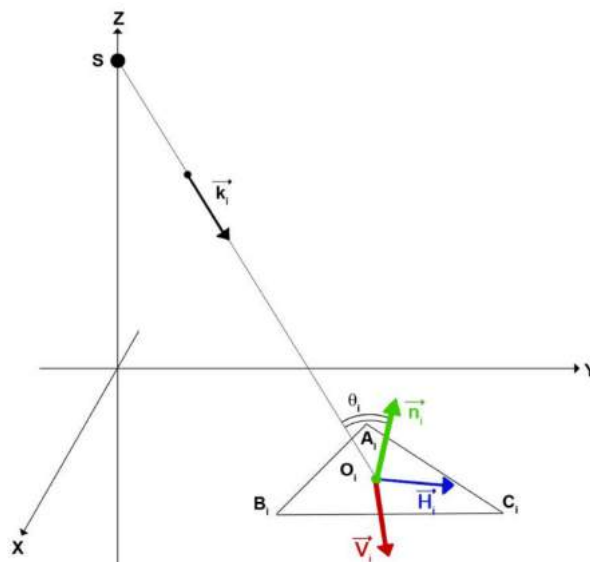


Figure 1. Forward Scattering Alignment (FSA) convention applied to an elementary triangle surface of the meshgrid used in the study.

The incident electric field is then projected on the unitary vectors \vec{H}_i and \vec{V}_i which form with \vec{k}_i a direct base. The \vec{H}_i vector is defined by:

$$\vec{H}_i = \frac{\vec{n}_i \wedge \vec{k}_i}{|\vec{n}_i \wedge \vec{k}_i|} = \begin{bmatrix} H_{Xi} \\ H_{Yi} \\ H_{Zi} \end{bmatrix} \quad (12)$$

where \vec{n}_i is the perpendicular vector to the elementary surface considered. The \vec{V}_i vector is defined as:

$$\vec{V}_i = \vec{H}_i \wedge \vec{k}_i = \begin{bmatrix} V_{Xi} \\ V_{Yi} \\ V_{Zi} \end{bmatrix} \quad (13)$$

The projection of \vec{E}_i on the (\vec{H}_i, \vec{V}_i) base is done through a scalar product:

$$E_{Hi} = \begin{bmatrix} E_{Xi} \\ E_{Yi} \\ E_{Zi} \end{bmatrix} \cdot \begin{bmatrix} H_{Xi} \\ H_{Yi} \\ H_{Zi} \end{bmatrix} \quad (14)$$

$$E_{Vi} = \begin{bmatrix} E_{Xi} \\ E_{Yi} \\ E_{Zi} \end{bmatrix} \cdot \begin{bmatrix} V_{Xi} \\ V_{Yi} \\ V_{Zi} \end{bmatrix} \quad (15)$$

Now the components of the incident electric field in terms of horizontal polarization H and vertical polarization V are known in the global set (O, X, Y, Z) . A local set is defined at the sample i with center O_i , vertical axis $O_i Z$ directed along the normal to the facet plane and horizontal axes in the sample plane. The vectors \vec{H}_i and \vec{V}_i are projected on the local polarization vectors \vec{H}_{il} and \vec{V}_{il} through a rotation matrix $[R]$.

The scattering matrix $[S]$ of the facet in the local set is defined as follows, with the backscattering coefficient σ_{HH} and σ_{VV} corresponding to the HH and VV polarizations respectively [33]. The ground cross-polarization is neglected in this study.

$$S = \begin{bmatrix} \sqrt{\sigma_{HH}} & 0 \\ 0 & \sqrt{\sigma_{VV}} \end{bmatrix} \quad (16)$$

The scattered electric field components towards the backscattering direction (same directions as \vec{H}_i and \vec{V}_i) are obtained as follows:

$$\begin{bmatrix} E_{Hsl} \\ E_{Vsl} \end{bmatrix} = S \cdot \begin{bmatrix} E_{Hil} \\ E_{Vil} \end{bmatrix} \quad (17)$$

The Equations (11)–(17) define the aspects relative to the electric field scattering. The local scattered field is afterward expressed in the global set, and then projected on the incident polarization. In order to take into account all factors impacting the attenuation amplitude of the EM field, a weighting coefficient is applied to the electric field for each elementary surface, corresponding to the attenuation factor present in the radar equation, and defined as follows:

$$C_i = \frac{A_i G^2 P \lambda^2}{R_i^4 (4\pi)^3} W(\theta_i) \quad (18)$$

where A_i is the elementary triangle area (see Appendix B), G the antenna gain, P the emitted power, λ the wavelength, R_i the distance between the antenna and the i th surface element (SO_i in Figure 1), $W(\theta_i)$ the antenna diagram used in the radar system (see Appendix C for the definition of the radar parameters).

The final electric field backscattered by the elementary surface following the X-, Y- and Z-axis is then determined by:

$$\begin{bmatrix} E_{XF_i} \\ E_{YF_i} \\ E_{ZF_i} \end{bmatrix} = E_{HS}C_i \begin{bmatrix} H_{Xi} \\ H_{Yi} \\ H_{Zi} \end{bmatrix} + E_{VS}C_i \begin{bmatrix} V_{Xi} \\ V_{Yi} \\ V_{Zi} \end{bmatrix} \quad (19)$$

A final phase component is added, taking into account the propagation term and a random phase Φ_i for removing the speckle component:

$$E_{Yi} = e^{-jk_iR_i+j\Phi_i} \quad (20)$$

The final electric field backscattered by the elementary surface is the complex sum of the fields scattered by all the facets.

2.2.2. Monopulse Waveform

When reaching the surface, the electric field is reflected and partly backscattered to the satellite following a power distribution, function of time. This power distribution of the radar echo is known as an altimeter waveform. The received power is sampled in time gates, each of them integrating the backscattered power during its aperture time. The contribution of each portion of the illuminated surface is received at a different time related to the topography of the surface (Figure 2). Based on the distance between the satellite and the surface, the recording of any individual waveforms starts when the first backscattered signal reaches the satellite position. The backscattered signal is sampled in a collection of time gates. The time gates have a duration (d_{gate}) of length τ , function of the radar system bandwidth B_w , as defined in [34]:

$$d_{gate} = \tau = \frac{1}{B_w} \quad (21)$$

Each elementary surface backscatters an electric field towards the satellite, which arrives at time t_i after the emission time t_0 . The three components of the waveform (WF) for any gate n can be expressed as:

$$WF_X(n) = \sum_{t_i=T_{n-1}}^{T_n} |E_{XF_i}(t_i)|^2, WF_Y(n) = \sum_{t_i=T_{n-1}}^{T_n} |E_{YF_i}(t_i)|^2, WF_Z(n) = \sum_{t_i=T_{n-1}}^{T_n} |E_{ZF_i}(t_i)|^2 \quad (22)$$

where T_{n-1} and T_n are the starting and ending times of the gate n .

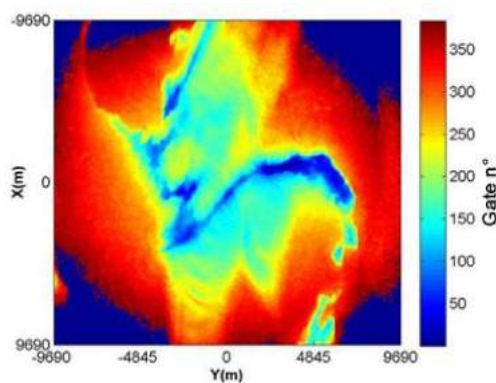


Figure 2. Example of modeled surface. The colors correspond to the corresponding radar time gate (here for 384 time gates).

Each waveform corresponds to a duration of a few milliseconds (a typical time gate lasts a few nanoseconds). The number of time gates generally varies from 64 to 128 on the current satellite altimeters and corresponds to the duration of the reception mode of the radar altimeter sensor. The opening of the reception window of the radar altimeter sensor is based either on the series of estimated ranges from a series of previous echoes (closed-loop mode) or, on the most recent altimetry missions, is forced by an estimate of the range based on a DEM to limit the problem of non-detection of open water targets as rivers flowing at the bottom of narrow valleys (open-loop mode, see [35] for more details). The altimeter waveform model developed in this study does not take into account these modes of operation. It is necessary to select n time gates over all the possible responses to obtain the individual altimeter waveform (red square on Figure 3). In order to calculate the backscattered power at a particular time of interest, a time lag variable is introduced corresponding to the switch of the sensor to the reception mode (see Figure 3). This time lag is determined manually by seeking the maximum cross-correlation between modeled and measured waveforms using 512 time-gate samples. The retained time-lag value for each site is then used for modeling the proper 128 time-gates waveforms.

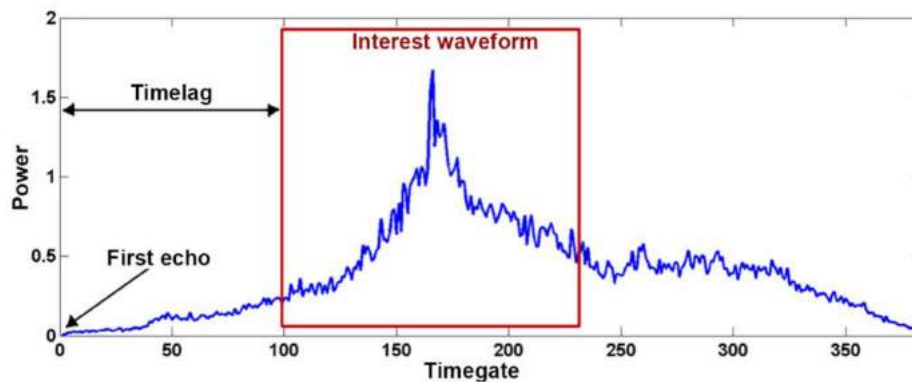


Figure 3. Example of a “raw” waveform simulated using the Continental waveform ALtimetry Model (CALM). We show the position of the first return signal, the time lag duration, and the interest waveform window (here composed of 128 points).

For each one of these time gates, the 3 components of the electric fields corresponding to the elementary surfaces whose surface-altimeter travel time corresponds to the gate’s time interval are added. Finally, for each gate, the total complex electric field is multiplied by its conjugate to obtain the power received by the altimeter for an individual waveform.

2.2.3. Averaged Waveform

In order to model as precisely as possible the satellite’s orbit impact on the radar measurement, the satellite movement on its orbit was taken into account. From the satellite’s orbit speed, which can be approximated as a radial speed, the satellite’s movement is simulated. In the model, Earth surfaces are represented using a planar approximation that is acceptable considering the dimension of the surfaces used in the simulation (a couple of tenths kilometers by a couple of tenths kilometers typically). The satellite’s movement can be assumed as a one dimension translation, following the Y-axis in CALM (see Appendix B).

The radar altimetry systems on orbit operate continuously along their tracks. The emission of the EM wave towards the surface is regularly performed according to the pulse repetition frequency. The pulse duration itself depends on the radar system parameters, and is different from one satellite to another. The repetition frequency, along with the satellite’s orbit speed, not only provides the apparent satellite ground speed, but also the ground space between two consecutive altimetry measurements.

During the backscattering process of the electromagnetic field, some of the coherent reflections vary much from one measurement to another during the satellite’s movement. Thus it is preferable to

make an average over a similar surface of many consecutive waveforms, which from a statistical point of view measure very similar surfaces. That is the procedure made onboard of both satellites, except for the “burst mode”. Examples of simulated waveforms taken from a series of consecutive 100 modeled radar echoes are presented in Figure 4a. The corresponding average waveform is presented in Figure 4b.

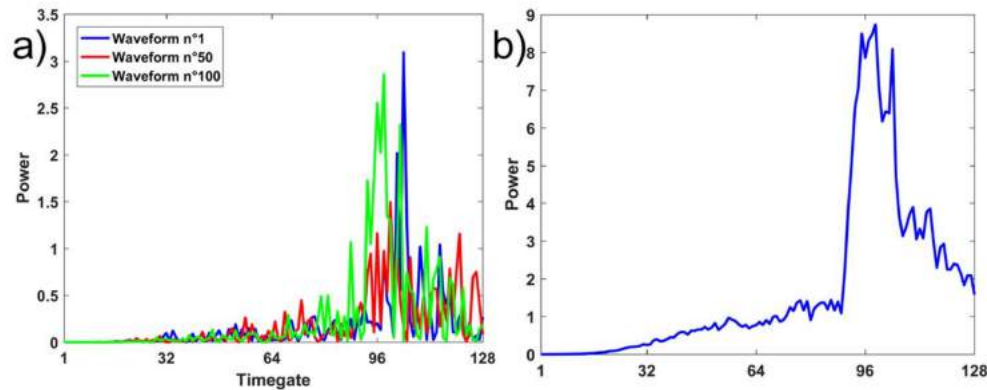


Figure 4. (a) Three examples of simulated waveforms (numbers 1, 50 and 100) taken from a series of consecutive radar echoes; (b) Mean waveform obtained averaging 100 simulated burst echoes.

3. Datasets

3.1. Radar Altimetry Data

Radar altimetry data used in this study comes from the acquisitions on the nominal orbit of the following missions: ENVISAT (2002–2010) and SARAL (2013–2016). These two satellites orbited a sun-synchronous polar orbit at an altitude of about 800 km, with a 35-day repeat cycle and an inclination of 98.6° , providing observations of the Earth from 81.5° latitude North to 81.5° latitude South, with a ground-track spacing of around 80 km at the Equator. RA-2, onboard the European Space Agency (ESA) ENVISAT mission, is a nadir-looking pulse-limited radar altimeter operating at Ku- (13.575 GHz) and S- (3.2 GHz) bands. The latter is available until January 2008, and is not used in the present study. SARAL is a CNES-ISRO joint-mission that was launched on 25 February 2013. Its payload is composed of the AltiKa radar altimeter and bi-frequency radiometer, and a triple system for precise orbit determination: the real-time tracking system DIODE (Détermination Immédiate d’Orbite par Doris Embarqué—Immediate Onboard Orbit Determination by Doris) of the DORIS (Doppler Orbitography and Radio-positioning Integrated by Satellite) instrument, a Laser Retroreflector Array (LRA), and the Advanced Research and Global Observation Satellite (ARGOS-3). It is the first altimeter to operate at Ka-band (35.75 GHz). The main characteristics of RA-2 and AltiKa are summarized in Table 1.

The Sensor Geophysical Data Records (SGDRs) delivered by CNES and ESA include accurate satellite positions (longitude, latitude and altitude of the satellite on its orbit) and timing, altimeter ranges, instrumental, propagation and geophysical corrections applied to the range, measured waveforms, and several other parameters such as the backscattering coefficients. These parameters are available at high frequency (i.e., 18 and 40 Hz for ENVISAT and SARAL data respectively). The waveforms from ENVISAT RA-2 at Ku band are sampled on 128 timegates, whereas waveforms from SARAL/AltiKa are sampled on 116 timegates. In this study, data from cycles 75 to 85 of ENVISAT RA-2 (January–December 2009) and cycles 1 to 35 (from February 2013 to June 2016) for SARAL AltiKa. These data were made available by the Centre de Topographie des Océans et de l’Hydrosphère (CTOH) [36].

Table 1. Main characteristics of ENVISAT and SARAL altimetry missions and of RA-2 and AltiKa sensors from [37,38].

	ENVISAT RA-2	SARAL AltiKa
Mean satellite altitude (km)	800	800
Velocity on orbit (km s ⁻¹)	7.45	7.47
Apparent ground velocity (km s ⁻¹)	6.62	6.64
Frequency bands	Ku (13.575 GHz), S (3.2 GHz)	Ka (35.75 GHz)
Pulse duration (chirp sweep time) (μs)	20	110
Effective pulse duration (ns)	3.125	1
Bandwidth (MHz)	320, 80, 20 (Ku) 160 (S)	500
Pulse repetition frequency (Hz)	1795 (Ku) 449 (S)	~3800
Time between two pulses (T, en μs)	557 (Ku) 2230 (S)	~263

3.2. ASTER DEM

ASTER is a Japanese sensor which is one of the five instruments onboard the Terra satellite, launched in 1999 by the NASA in low Earth orbit. It has collected ground data since February 2000. ASTER provides high-resolution images of the Earth in 14 bands of the electromagnetic spectrum, from the visible domain to the thermic infrared. The resolution of these images varies between 15 m and 90 m. Data from ASTER are used to create detailed maps of the surface temperature, emissivity, reflectance, and what is of interest to us, maps of elevation.

The first version of the ASTER Global Data Elevation Model (GDEM), which was released in 2009, has been generated using stereoscopic images collected by the instrument. The global coverage was extending from 83°S to 83°N, covering 99% of the global continental surface. The second version [37] added 260,000 stereoscopic images to the previous version, improving the global coverage and reducing the number of artefacts. The data production algorithm provides a better spatial resolution, an improved horizontal and vertical precision, along with an improved water surfaces coverage. The distributed data format remains GeoTIFF, and the same sampling grid is used, with a resolution of 30m and cells of 1° × 1°. ASTER GDEM data are freely available worldwide. They can be downloaded from the internet on the Land Processes Distributed Active Archive Center (LP DAAC) (<https://lpdaac.usgs.gov/>).

4. Study Area

The selected sites are distributed along a north-south rainfall gradient in the Gourma region, Mali in the west-African Sahel. The Gourma region (14.5–17.5°N and 1–2°W), is a vast peneplain at between 250 and 330 m altitude and has been previously used by numerous remote sensing studies, based on active and passive microwave sensors (e.g., [7,9–11,18,19,21]). Indeed, the presence of large homogeneous and flat surfaces characterized by a high seasonal and inter-annual variability makes this region particularly well suited both for methodological development and for multi-product validation exercises [39]. Predominantly sandy (58% of the region) or shallow (23%) soils are distributed in large alternant swaths of contrasted land cover (fixed sand dunes, eroded surfaces locally capped by iron pan). Besides these two major landforms, remnants of alluvial systems and lacustrine depressions form a web of narrow bands often slotted in between sandy and shallow soils [39]. In this region, the mean annual rainfall varies between 150 and 400 mm from north to south with interannual variations ranging between 15 and 30% of the annual rainfall. Rainfall occurs during the northern hemisphere summer, starting between May and July until September or October with a maximum in August [40].

Five study sites are selected on the 302, 373 and 846 ground tracks of ENVISAT and SARAL altimeters (see Figure 5). The site 1 is located on SARAL/ENVISAT track 846. The satellite goes from north to south over the reference point at latitude 16.75°N and longitude 1.842°W, at the north of the In Zaket area. This site presents mostly sand dunes along with some rock formation in the center of the area. At the east of the site, the beginning of a great dune can be seen. No open water surface is present here.

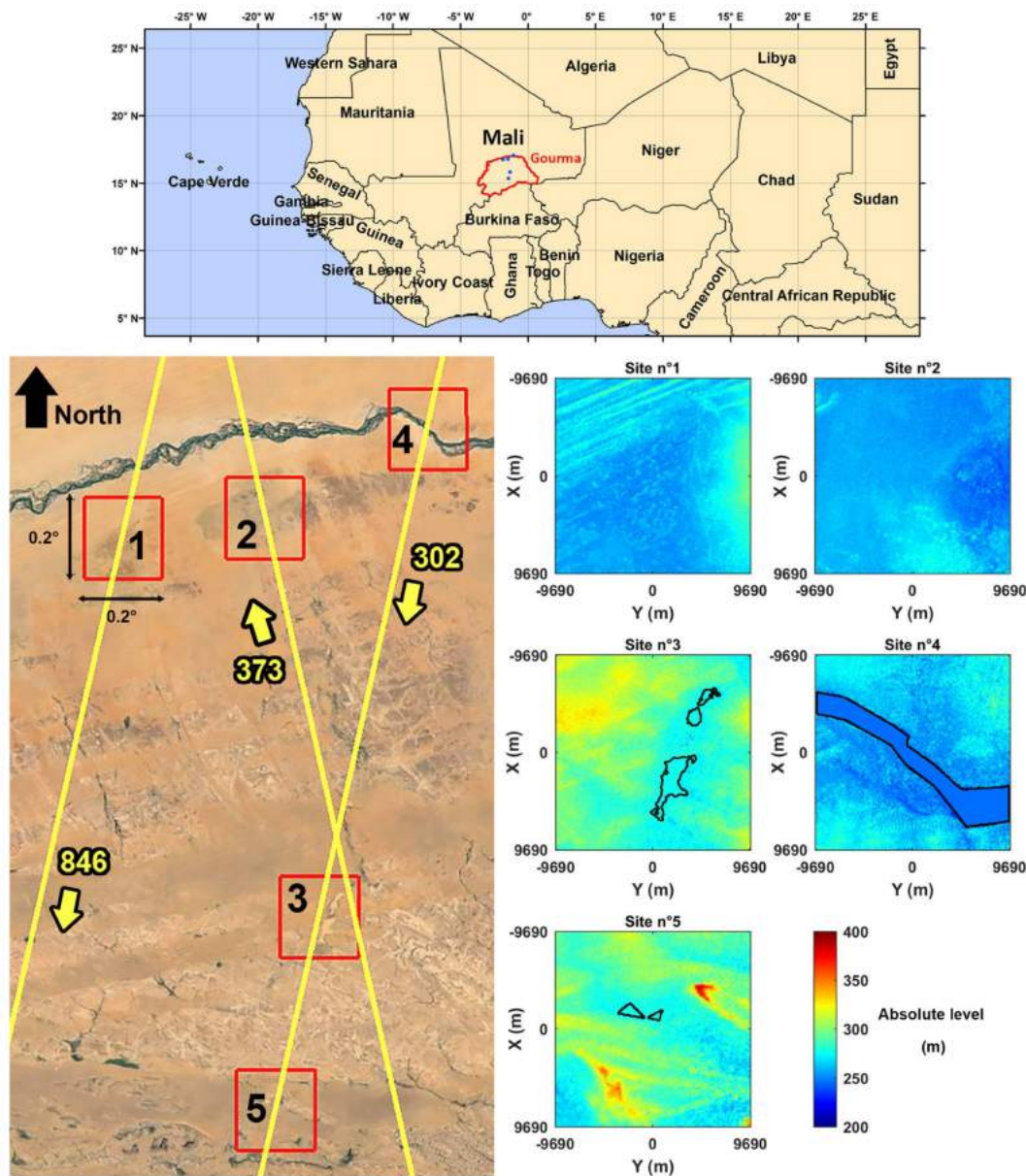


Figure 5. Location of the five study sites distributed on satellite tracks 302, 373 and 846 of ENVISAT/SARAL over the Gourma region, Mali © Google Earth. The azimuthal direction of the satellite on orbit, the site numbers and the corresponding DEM extraction area are indicated. The water areas limits over each site are marked with black lines.

Site 2 is located on SARAL/ENVISAT track 373, with the satellite going from south to north. The reference point is at latitude 16.8°N and longitude 1.478°W. The site is a sandy plane with nearly no dune pattern. No open water surface is present in this area.

Site 3 is located on SARAL/ENVISAT track 302, close to the Gossi village. The satellite goes from north to south over the latitude 15.82°N and longitude 1.339°W reference point. The site presents mainly sand dunes, which in the center presents a structure of three ponds along with a flood area in the southern part. The DEM has been reworked to simulate these water ponds by quadrangular areas, with heights of 278 m, 277 m and 275 m from north to south respectively.

Site 4 is located at coordinates 17.02°N and 1.059°W on the SARAL/ENVISAT track 302. The site is composed of a sandy soil, through which flows the Niger River from northwest to southeast of the

extraction area (see Figure 5). The Niger River is simulated by six quadrangular areas at the same altitude of 245 m, which is considered to be the height of the high river bed at the end of the monsoon.

Site 5, located on SARAL/ENVISAT track 302, is close to the Agoufou pond. With coordinates of 15.345°N and 1.45°W, this sandy plain with dune formations presents a pond composed of two triangular areas (see). These two ponds are simulated by two triangular areas with the same altitude of 275 m. A rocky peak at the northeast of this area (the red “V” on Figure 5) implies adding a consequent time-lag on the waveform formation.

5. Results

5.1. Comparison between Simulated and Real Waveforms

Radar altimetry waveform simulations were performed over the five sites presented in Section 4. Study area for both ENVISAT RA-2 and SARAL AltiKa missions. The representation of the scene is described in Appendix D. Parameters used in this study are presented in Appendix E. As no information on the power amplification applied to the received signal in the electronics onboard the satellites is available, an empirical gain determination was applied (see Appendix F).

Radar altimetry waveforms were simulated for the dry season (i.e., SSM = 0.02) over the five test sites for both ENVISAT RA-2 and SARAL AltiKa missions. They were compared to radar altimetry waveforms present in the SGDR. The real waveforms were selected at the closest acquisition location to the reference location of the test sites. As the orbit slightly change with time, the footprint center is not exactly the same from one cycle to another, the scene encompassed is different.

In our study, ENVISAT RA-2 measurements for the thirty-five chosen cycles, corresponding to the dry season from January to May, are close to the reference point and, are encompassed in a circle of 500 m of radius. SARAL/AltiKa are more scattered, within a 2500 m buffer along the nominal orbit track. This deviation is similar for the five study sites, and introduces variations on each waveform observed. These variations are limited for ENVISAT data, the footprints being similar between measurement times. The impact on SARAL/AltiKa data is stronger, seeing that a distance of 2500 m between two different footprints implies that only 60% of the same scene is observed. Finally, the selected waveforms were averaged over the whole period of observation for each satellite. The resulting averaged waveforms are presented in Figure 6.

An overall good agreement is found between the averaged observed waveforms and the simulated ones with correlation ranging from 0.66 to 0.94 at Ku-band for ENVISAT RA-2 and from 0.27 to 0.96 at Ka-band for SARAL/AltiKa. Over site 1 at Ku-band, both simulated and real waveforms have a similar shape with a correlation coefficient of 0.94. On the same site at Ka-band, the modeled waveform presents a slower increase of the leading edge contrary to the average of real waveforms, but with a similar trailing edge. The correlation coefficient between simulated and waveforms is of 0.96. Over site 2, both simulated and averaged observed waveforms have close profiles at Ku and Ka-bands with correlation coefficients of 0.91 for both bands. However, the simulated waveform has a much lower amplitude (150 against 400) at Ka-band compared to Ku-band. Over site 3, both simulated and real waveforms are very similar until gates 80 at Ka-band and 90 at Ku-band. After those time gates, the modeled waveforms present a huge peak at both Ku and Ka-bands which is not present in the average measured waveforms. This peak is due to the presence of temporary ponds in the scene. The issue of the pond levels, considered for the simulation as high and which is oppositely low for the dry season measured waveforms considered, leads to these differences and low correlation coefficient. Besides, due to the drifts of the satellite ground-track from one cycle to another, larger for SARAL than for ENVISAT, the location of the signature of the ponds also changes. Correlation coefficients of 0.66 and 0.27 were found at Ku and Ka-bands respectively. Over site 4, corresponding to the cross-section with the Niger River, the average of the observed radar echoes are very specular at both Ku- and Ka- bands. Very huge power is reflected by the surface of the river acting as a mirror at microwave frequencies. The modeled waveforms exhibit more important trailing edge slopes resulting

in larger radar echoes. This may result from issues in the modeling of water surfaces considered as flat surfaces, and hence neglecting the surface roughness responsible for the decrease of the signal aside from the nadir-looking angle. The correlation coefficients of 0.72 and 0.88 were found at Ku and Ka-bands respectively. Over site 5, the modeled and the average of the waveforms are characterized by one large (at Ka-band) or two peaks (at Ku-band) corresponding to the two small ponds present in the scene. The correlation coefficients are of 0.88 and 0.79 at Ku and Ka-bands respectively. As it can be seen in Figure 6, important changes in amplitude can be observed from one cycle to another, that cannot be attributed neither to the filling of the temporary ponds nor to the drift in the altimeter orbits.

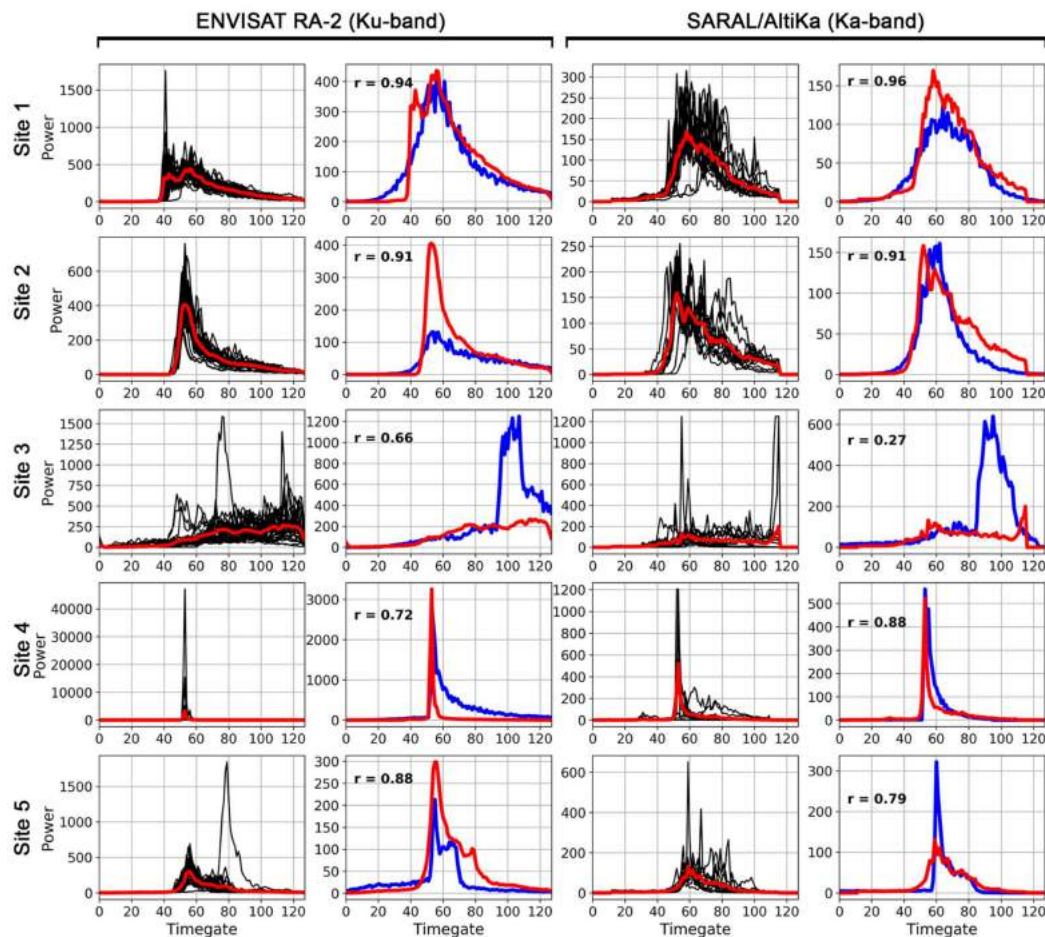


Figure 6. Individual (black) and mean (red) waveforms on the five study sites over the observation periods from ENVISAT RA-2 at Ku-band (left of the left panel) and from SARAL/AltiKa at Ka-band (left of the right panel). Comparison over the five study sites between the modeled waveform (in blue) and the mean observed waveform (in red), with the correlation coefficient r indicated from ENVISAT RA-2 at Ku-band (right of the left panel) and from at SARAL/AltiKa at Ka-band (right of the right panel).

5.2. Impact of Surface Soil Moisture on Altimetry Signal

Previous studies showed that the temporal variations in SSM in semi arid areas have a strong impact on the radar altimetry backscattering coefficients reaching up to 25–30 dB between the dry and the wet seasons [20–25]. Over the five sites considered previously, new simulations were run at Ku and Ka-bands considering the following values of SSM: 0.05, 0.1, 0.2, 0.3 and 0.4 that encompass the range of SSM variations in the Gourma region of Mali. The backscattering coefficients derived from the modeled waveforms were also estimated. Following [20–25], backscattering coefficients were derived

using the Offset Center of Gravity (OCOG) or Ice-1 retracking algorithm [41] that is commonly used for the application of satellite altimetry to land hydrology [42]. The results of these simulations are presented in Figure 7 along with the variations of the backscattering coefficient against SSM.

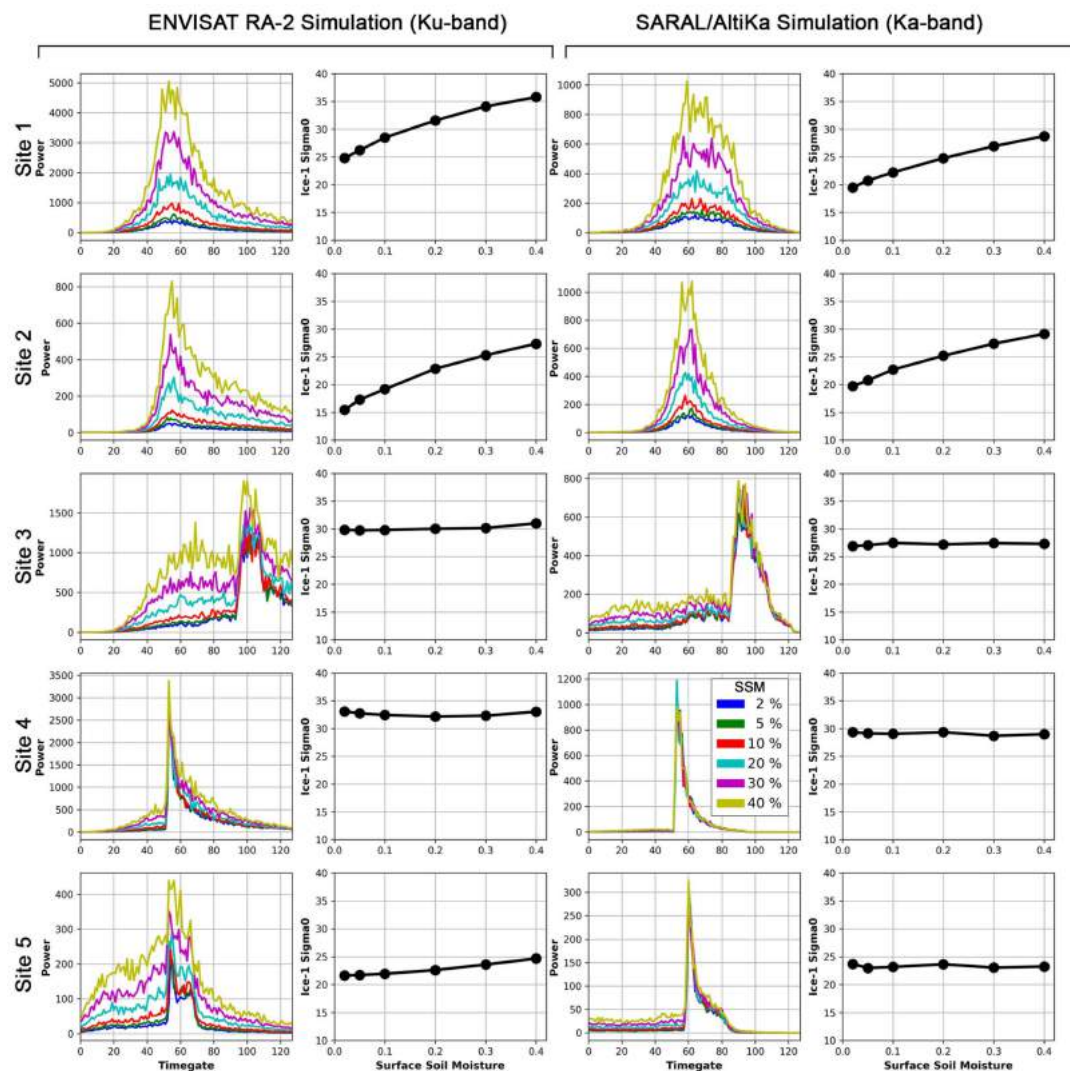


Figure 7. Simulated waveforms for increasing values of surface soil moisture (SSM) (2%—blue, 5%—green, 10%—red, 20%—light blue, 30%—purple, 40%—yellow) on the five study sites at Ku-band (left of the left panel) and at Ka-band (left of the right panel). Corresponding backscattering coefficients (dB) as a function of SSM (%) at Ku-band (right of the left panel) and from at Ka-band (right of the right panel).

The amplitude of the simulated waveforms rises with increasing SSM over sandy sites without water (sites 1 and 2), at both Ku and Ka-bands. The amplitude of the maximum of the waveform is multiplied by a factor between 5 and 8 at Ku-band and between 4 and 6 at Ka-band for variations in SSM between 0.1 and 0.4. Backscattering values range from ~25 to ~35 dB over site 1 and from ~15 to ~30 dB over site 2 at Ku-band, and from ~20 to ~30 dB over the two sites at Ka-band. These results are in good agreement with what was observed in earlier studies [20–25]. Nevertheless, lower values of backscattering during the dry season and higher amplitude would have been expected at Ka rather than at Ku band. This discrepancy is likely to be due to (i) the configuration of the scenes that are not homogeneous; (ii) the extension of the semi-empirical model of the soil complex permittivity at

Ka-band that is not completely valid; and (iii) the values of the correlation length and of the RMS of the roughness height that are not completely adequate, especially at Ka-band (see Appendix E).

Over site 4, corresponding to the presence of the Niger River in the scene, the radar echo is dominated the peaky waveform corresponding to the signature of the river. Increases in returned power are observed on the sides of the peak corresponding to changes in SSM on the river banks. They are negligible compared with the value of the maximum observed at the peak. As a consequence, the backscattering coefficient is constant for any value of the SSM and equals to ~35 dB at Ku-band and ~30 dB at Ka-band. Please note that the width of the Niger River remains constant for all the simulations, i.e., effects of the flood were not taken into account. An increase of the width of the river would have caused an increase in the backscattering coefficient at both bands, as observed in [23].

The configuration of sites 3 and 5 leads to a mix between the two former situations. The ponds, considered permanent, and hence present in all the simulations, occupy a smaller surface than the Niger River in site 4. As a consequence, the amplitude of the simulated waveforms rises over all the gates, even the ones corresponding to the ponds (i.e., from gates 95 to 100 and from gates 80 to 110 over site 3, from gates 50 to 75 and from gates 60 to 85 at Ku and Ka-bands respectively) with increasing SSM. However, the backscattering coefficient remains almost constant and equals to ~30 dB (with slight increase at ~31 dB for SSM equals 0.4) and ~25 dB at Ku and Ka-bands respectively over site 3, almost constant and equals to ~24 dB at Ka-band over site 5, with a slight increase from ~21 to ~24 dB at Ku-band over site 5. The reason for these lacks of change in the backscattering coefficient with SSM when the radar altimetry waveforms are impacted is due to the retracking algorithm. In the case of OCOG/Ice-1, the waveform is simulated by a rectangular box encompassing the maximum of the power returned. Over the two sites, the box width corresponds to the extent of the signature of the small ponds. Most of the increase of the SSM on the backscattered power is filtered out. As a consequence, the backscattering coefficient is almost constant. This is the reason why, the measurements contaminated by temporary floods were excluded from SSM inversion by [21].

6. Conclusions

This study analyzed the impact of SSM on the radar altimetry waveform over semi-arid areas, and as a consequence, on radar altimetry backscattering coefficient through a modeling approach. A two-scale model, coupled with a semi-empirical model for the complex dielectric permittivity of the soil, was applied to simulate the altimetry radar echoes at Ku and Ka-bands through an approach taking into account the surface roughness (microscopic scale) and the surface topography (macroscopic scale). Comparisons between simulated and real waveforms from ENVISAT RA-2 and SARAL AltiKa acquired at Ku and Ka-bands show a good agreement with correlation ranging from 0.66 to 0.94 at Ku-band and from 0.27 to 0.96 at Ka-band over the five study sites representative of the Sahelian zone of Gourma in Mali. Increase in SSM over typical range of variations in semi-arid conditions (from 0.02 to 0.4), show a rise of the power received by the altimeter over sandy areas that causes a raise of 10 to 15 dB of the backscattering coefficient. Such large changes can be observed when the radar altimeter made its acquisitions a short time after an intense rain event. The presence of open water in the scene observed by the altimeter (river and even small ponds) cancelled the effect of the increase in SSM. The waveform is dominated by the peak corresponding to the presence of open water, especially in the case of a large river such as the Niger. As the retracking algorithm derives the waveform parameters from this peak, including the backscattering coefficient, changes in SSM are negligible compared with the presence of open water. These results are in good agreement with what was previously observed analyzing radar altimetry backscattering coefficients acquired over semi-arid areas.

The modeling approach developed in this study (CALM) could benefit from the following improvements:

- (1) a more realistic description of the open water areas taking into account the small undulations of the surface as in [43],
- (2) accurate values of the roughness parameters at Ku and Ka-bands and their spatio-temporal variations over the study sites,
- (3) DEM at higher spatial resolution and with a better accuracy, to obtain more accurate simulation results.

The next steps would be the analysis of the impact of the vegetation on the simulation results and the application of this model to the SAR acquisition mode operating at low incidence angles and the comparisons to the Sentinel-3A data.

Acknowledgments: The authors were supported by CNES and ONERA through C.F PhD grant. They were also supported by by CNES/EUMETSAT Ocean Surface Topography Science Team (OSTST) through the funding of the “new Perspectives for higher Resolution Altimetry—a Multi-disciplinary approach (PRIAM)” project and by CNES TOSCA through the funding of the “Caractérisation des Surfaces Continentales par Altimétrie et Diffusiométrie (CASCAD)” project.

Author Contributions: C.F., P.B., F.F. and E.M. conceived and designed the study. C.F. performed the experiments. All the authors analyzed the data and contributed to the redaction of the paper.

Conflicts of Interest: The authors declare no conflict of interest. The founding sponsors had no role in the design of the study; in the collection, analyses, or interpretation of data; in the writing of the manuscript, and in the decision to publish the results.

Appendix A

The parameters of the soil complex dielectric permittivity model from [27,28] are detailed below. The effective free water permittivity ϵ_{fw} of the soil is defined as:

$$\epsilon_{fw} = \epsilon_{w\infty} + \frac{\epsilon_0 - \epsilon_{w\infty}}{1 + j2\pi f\tau} - j \frac{\sigma_{eff}}{2\pi f\epsilon_0} * \frac{\rho_s - \rho_b}{\rho_s * m_v} \quad (A1)$$

where f is the frequency of the electromagnetic wave emitted by the sensor, m_v is the volumetric soil moisture given in percent, The water dielectric permittivity for very high frequencies converge towards an “infinite” value $\epsilon_{w\infty}$ taken at $\epsilon_{w\infty} = 4.9$, ϵ_{w0} is the non-salted water permittivity for the null frequency estimated using the following equation [29]:

$$\epsilon_{w0} = 87.74 - 0.4008 * T + (9.398 \times 10^{-4}) * T^2 + (1.410 \times 10^{-6}) * T^3 \quad (A2)$$

T is the ground temperature in Celsius degrees, τ is the water relaxation time, which is also function of the temperature, and defined as follows:

$$2\pi\tau = (1.1109 \times 10^{-10}) - (3.824 \times 10^{-12}) * T + (6.938 \times 10^{-14}) * T^2 - (5.096 \times 10^{-16}) * T^3 \quad (A3)$$

σ_{eff} is the effective water conductivity in the ground, and depends on the soil bulk density ρ_b and on the sand and clay composition of the ground S and C :

$$\sigma_{eff} = -1.645 + 1.939\rho_b - 0.02013 * S + 0.01594 * C \quad (A4)$$

The relative dry soil permittivity ϵ_s is defined as:

$$\epsilon_s = (1.01 + 0.44\rho_s)^2 - 0.062 \quad (A5)$$

where ρ_s is the specific soil density defined as:

$$\rho_s = \frac{\rho_b}{1 - v_a} \quad (A6)$$

v_a is the void fraction of the ground (taken further on at 0.65), and ρ_b is the soil bulk density, in g/cm^3 . The shape constant (α) is further on taken at 0.65 and the empirical constant (β) is defined as:

$$\beta = \beta_r + j * \beta_{im} \tag{A7}$$

where

$$\beta_r = (127.48 - 0.519 * S - 0.152 * C) / 100 \tag{A8}$$

$$\beta_{im} = (1.33797 - 0.603 * S - 0.166 * C) / 100 \tag{A9}$$

Appendix B

In the Continental waveform ALtimetry Model (CALM), the surface illuminated by the EM wave emitted by the sensor (i.e., the radar altimeter footprint) is represented using a meshgrid of triangles. This meshgrid is considered uniform in both directions (X and Y-axis, see Figure A1). The altimetry backscattering is assumed to occur in a rectangular surface, which size is determined by the number of mesh N_x in the X-axis (a mesh corresponds to a basic elementary triangle) and N_y in the Y axis encompassing the theoretical altimeter footprint. The surface resolution R is then the distance between two consecutive meshes, taken in this study as constant in both axes. The surface parameters are defined in a matrix that has a $2N_x + 1$ by $2N_y + 1$ size representing each point position on the meshgrid (position in X and Y axis, point height in the Z axis and the surface of each triangle). The center of the matrix is the origin point of the coordinate system defined as the instant of emission of the EM wave for each measurement, and is located on the satellite groundtrack.

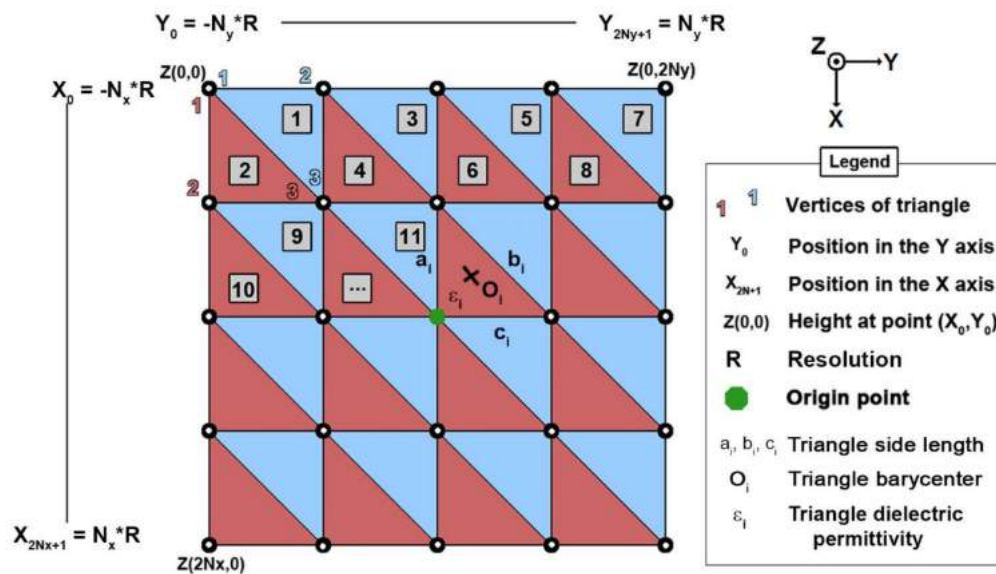


Figure A1. Meshgrid representing the coordinate system and norms used in CALM. In this example, $N_x = N_y = 2$.

Each elementary surface composing the meshgrid is characterized by the lengths a_i , b_i and c_i of the triangle sides and its barycenter O_i , as represented in Figure A1. By numbering each elementary surface, we create a matrix with—among other information—the coordinates of the triangles vertices and their surface, calculated from the Heron formula:

$$A_i = \sqrt{p_i(p_i - a_i)(p_i - b_i)(p_i - c_i)} \tag{A10}$$

where

$$p_i = \frac{1}{2}(a_i + b_i + c_i) \quad (\text{A11})$$

The perpendicular vectors to each triangle are determined using a normalized vectorial product. Each elementary surface is also attributed to a proper dielectric permittivity ε_{ri} , computed as explained in Section 2.1.2. In the different cases considered in this study, dielectric permittivity and roughness parameters (root mean square height, correlation function type and correlation length) have the same value for all the non-inundated grid elements at each time step.

Finally, each elementary surface is given an 11-variables vector:

- the mean X position (noted as X_i further on),
- the mean Y position (noted as Y_i further on),
- the mean Z position (noted as Z_i further on),
- the X axis component of the perpendicular vector (noted as N_x),
- the Y axis component of the perpendicular vector (noted as N_y),
- the Z axis component of the perpendicular vector (noted as N_z),
- the nature of the elementary surface (-1 for water, 0 for ground is the default value),
- the root mean square height hrms (noted as h_i),
- the surface correlation length (noted as l_i),
- the triangle area (noted as A_i),
- the surface complex dielectric permittivity (noted as ε_{ri}),

All these parameters characterize each elementary surface, and can be further on changed to attribute new properties to selected areas.

Appendix C

The antenna field of view depends on the wavelength λ and the antenna diameter D , and is expressed in radians by the following formula:

$$\theta_{3\text{dB}} = \frac{70\lambda\pi}{D180} \quad (\text{A12})$$

Knowing this antenna field of view and the distance between the satellite orbit and the ground, the observed ground area can be limited to a disc of radius corresponding to the observable ground, given by the 3 dB power attenuation.

The antenna gain is expressed by:

$$G = \frac{4 \log(2)}{\theta_{3\text{dB}}^2} \quad (\text{A13})$$

Taking into account the antenna diagram, the ponderation is then defined as:

$$W(\theta) = \exp(-2G\theta) \quad (\text{A14})$$

Appendix D

The definition of the simulation scene is composed of three main steps: the resizing of the DEM data according the altimeter footprint, the delineation of open water areas present in the scene and the orientation of the scene depending whether the altimetry tracks are ascending or descending.

- Resizing of the DEM

This first step allows to take into account the different altimeter footprint sizes (see Figure A2), the location of the open water surfaces, and to improve the computation time. As the extracted gridded ASTER DEM data are provided by tiles of $1^\circ \times 1^\circ$, each tile largely encompasses the size of an individual altimeter footprint. For each individual footprint, the DEM is cropped to encompass the altimeter footprint in the square of minimum area containing it. For instance, using the 30 m resolution GDEM ASTER data, and for an ENVISAT RA-2 simulation at Ku-band, a square of $N_x = N_y = 646$ grid elements is selected. This implies corresponds to a scene of 19,380 m, to be compared with the approximated 18,000 m footprint diameter of ENVISAT RA-2 at Ku-band (see the example in Figure A3).

- Delineation of surface water extent

Water surface extent in the study areas were delineated using Google Earth and added to the scene. As the elevation of this surface is often non-uniform in the DEM, the lowest elevation in this area and its surroundings is attributed to the whole open water area (see Figure A4). As many information on these surfaces is missing, a default backscattering coefficient of 17 and 20 dB at Ku and Ka bands respectively was attributed. Those values correspond to the mean backscattering value over the Niger River at both bands.

- Orientation of the scene

In CALM, the orbit trajectory is considered linear following the Y-axis of the modeled surface. The original DEM extraction is orientated with the North as the top of the extraction area. To take into account the satellite movement on orbit it is then necessary to apply a surface rotation of 90° , clockwise for a movement from south to north, and anticlockwise from north to south (green arrow in Figure A2). The real and simulated orbits are not exactly in the same direction, but rather present an angle with the meridian. Rigorously, the rotation of the observed area should respect the same angle to be in the same measurement conditions. Nevertheless, over a hundred successive measurements, the satellite ground movement does not exceed 500 m, for a footprint diameter going from 8 km to 18 km for the considered altimetry satellites. The error on orbit simulation is considered as negligible.

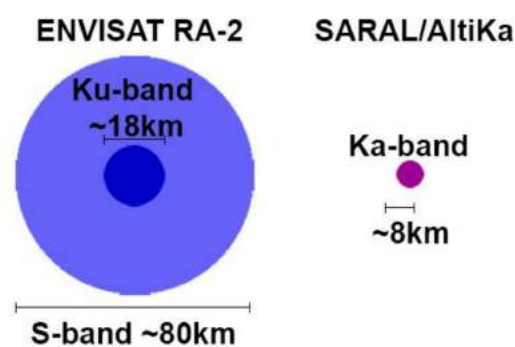


Figure A2. Size of the theoretical footprints for a totally plane surface as a function of the frequency used for ENVISAT RA-2 and SARAL AltiKa.

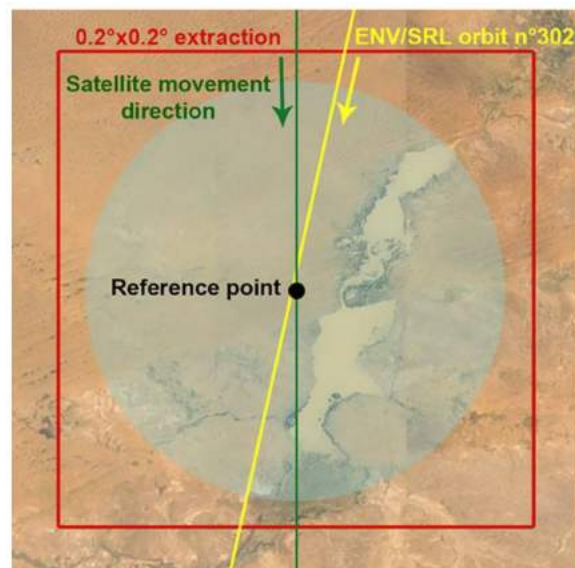


Figure A3. Example of a scene using ASTER GDEM data centered close to the Gossi pond in Mali. The real altimeter satellite path 0302 of ENVISAT RA-2 is represented in yellow, and the simulated orbit (green), along with the reference point of the simulation. The shadowed area around the reference point corresponds to the Ku-band footprint of ENVISAT RA-2.

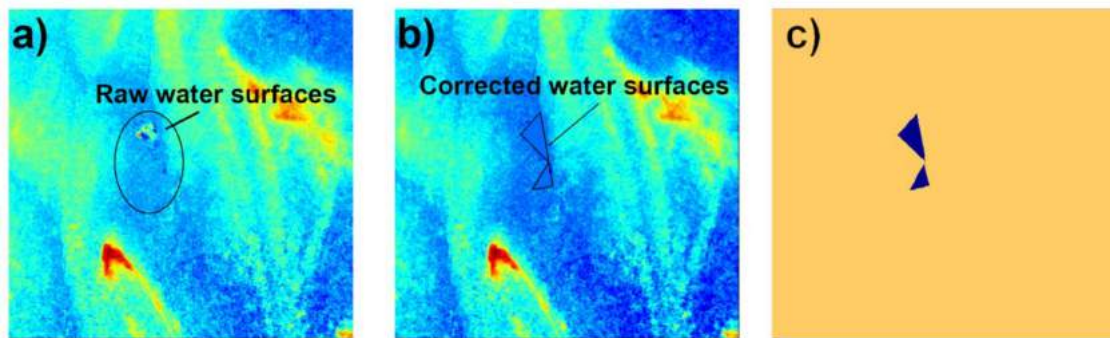


Figure A4. Example of processing applied to surfaces with water areas. (a) The raw DEM without any water surface treatment; (b) DEM with corrected water surfaces; (c) Surface nature as entered in CALM (water in blue, ground in orange).

Appendix E

All the parameters used in the CALM simulation for ENVISAT RA-2 at Ku-band and SARAL/AltiKa at Ka-band are listed in Table A1.

Table A1. Main characteristics of ENVISAT and SARAL altimetry missions and of RA-2 and AltiKa sensors from [37,38].

	ENVISAT RA-2	SARAL AltiKa
Mean satellite altitude (km)	800	800
Velocity on orbit (km s ⁻¹)	7.45	7.47
Apparent ground velocity (km s ⁻¹)	6.62	6.64
Frequency bands	Ku (13.5 GHz), S (3.2 GHz)	Ka (35.5 GHz)
Pulse duration (chirp sweep time) (μs)	20	110
Effective pulse duration (ns)	3.125	1
Bandwidth (MHz)	320, 80, 20 (Ku) 160 (S)	500
Pulse repetition frequency (Hz)	1795 (Ku) 449 (S)	~3800
Time between two pulses (<i>T</i> , μs)	557 (Ku) 2230 (S)	~263
Antenna parabola diameter (m)	1.2	1
Footprint diameter (km)	~18	~8
Antenna gain	37 dB	44 dB
Emitted power (W)	161	100
Distance between two consecutive measurements	3.69 m	1.66 m
Void fraction (v_a)		0.36
Sand ground component S		60
Clay ground component C		20
Soil bulk density (rb)		1.69
Alpha parameter		0.65
Temperature (°C)		30
Correlation length		4.5 cm
Height rms (roughness)		0.35 cm

Very few in situ data are available over this area for the roughness parameters (hrms, correlation length). The roughness data were measured at the Agoufou site in August 2005 (60 profiles) and February 2006 (16 profiles) in the heart of the wet and dry seasons respectively [19]. These data were obtained using a 2 m-long profilometer linear needle roughness device, which needles are separated from one another by 1 cm, allowing the estimation of standard deviation of roughness heights and the autocorrelation length. The mean values determined over the Agoufou site allowed to estimate a mean hrms height of 0.7/0.5 cm, for a mean correlation length of 12.6/13.5 cm during the dry and the rainy seasons. The 1 cm separation length between two needles is too long for Ku (2.3 cm of wavelength) and Ka (0.8 cm wavelength) bands. As these in situ roughness values cannot be used in this study, roughness parameters determined in [26] for dry and smooth sandy soils similar to the Gourma soil types (hrms of 0.35 cm and correlation length of 4.5 cm). Due to the limited anthropogenic impact in this region, the ground is considered Gaussian. Using this values, the validity of the assumptions allowing the use of this GO model were checked (Table A2). All the criteria are validated at Ka band, and 2 out of 3 at Ku-band, except $k_s > 1.5$.

Table A2. Variables used for the validity of the GO model.

	Ku Band	Ka Band
kl (rad)	12.72	33.46
l^2 (10 ⁻³ m ²)	2.0	2.0
$2.67s\lambda$ (10 ⁻³ m ²)	0.21	0.08
k_s (rad)	0.99	2.60

Appendix F

The electronic systems onboard the satellites contain amplifiers that increase the power of received electromagnetic signal, strongly attenuated after 1600 km of propagation. No information concerning the amplifiers onboard the satellites is available. In order to take into account the amplification gains, the Automatic Gain Control (AGC) and the system calibration on the waveforms modeled with CALM to compare them with real satellite waveforms, a gain factor is applied. This gain is determined empirically to make for the simulated waveforms to correspond to the mean measured satellite waveform over the observation periods (11 cycles for ENVISAT, 18 for AltiKa). Along with the added time lag, this leads to a decent waveform modeling with the proper timeframe.

Table A3 shows that the empirical gain to apply is important. It remains though quite constant for each satellite (only a maximum 10 dB difference). Of course, this gain is insufficient to provide precise modeling, but this method has proven to give satisfactory results. The time lag is inherent to each observed surface, and thus varies strongly from one site to another. In order for the modeled waveform to correspond to the mean measured waveform, the time-lag has been determined using cross-correlation maxima.

Table A3. Empirical gains and time lags applied to each study site for both ENVISAT RA-2 and SARAL/AltiKa configurations.

Simulation Site	ENVISAT RA-2		SARAL/AltiKa	
	Empirical Gain (dB)	Timelag (ns)	Empirical Gain (dB)	Timelag (ns)
Site 1	343.42	0	339.03	33
Site 2	337.78	−30	336.53	18
Site 3	341.76	35	336.02	158
Site 4	339.03	100	327.78	160
Site 5	335.44	425	330	164
Mean	340.37	n/a	335.59	n/a
STD	2.28	n/a	2.62	n/a

References

- Koster, R.D.; Dirmeyer, P.A.; Guo, Z.; Bonan, G.; Chan, E.; Cox, P.; Gordon, C.T.; Kanae, S.; Kowalczyk, E.; Lawrence, D.; et al. GLACE Team Regions of strong coupling between soil moisture and precipitation. *Science* **2004**, *305*, 1138–1140. [[CrossRef](#)] [[PubMed](#)]
- Entekhabi, D.; Rodriguez-Iturbe, I. Analytical framework for the characterization of the space-time variability of soil moisture. *Adv. Water Resour.* **1994**, *17*, 35–45. [[CrossRef](#)]
- Small, E.E.; Kurc, S.A. Tight coupling between soil moisture and the surface radiation budget in semiarid environments: Implications for land-atmosphere interactions. *Water Resour. Res.* **2003**, *39*. [[CrossRef](#)]
- Mott, J.J. Factors Affecting Seed Germination in Three Annual Species from an Arid Region of Western Australia. *J. Ecol.* **1974**, *62*, 699. [[CrossRef](#)]
- Delon, C.; Mougin, E.; Serça, D.; Grippa, M.; Hiernaux, P.; Diawara, M.; Galy-Lacaux, C.; Kergoat, L. Modelling the effect of soil moisture and organic matter degradation on biogenic NO emissions from soils in Sahel rangeland (Mali). *Biogeosciences* **2015**, *12*, 3253–3272. [[CrossRef](#)]
- Wagner, W.; Lemoine, G.; Rott, H. A Method for Estimating Soil Moisture from ERS Scatterometer and Soil Data. *Remote Sens. Environ.* **1999**, *70*, 191–207. [[CrossRef](#)]
- Jarlan, L.; Mougin, E.; Frison, P.L.; Mazzega, P.; Hiernaux, P. Analysis of ERS wind scatterometer time series over Sahel (Mali). *Remote Sens. Environ.* **2002**, *81*, 404–415. [[CrossRef](#)]
- Gruhler, C.; de Rosnay, P.; Kerr, Y.; Mougin, E.; Ceschia, E.; Calvet, J.C.; Richaume, P. Evaluation of AMSR-E soil moisture product based on ground measurements over temperate and semi-arid regions. *Geophys. Res. Lett.* **2008**, *35*. [[CrossRef](#)]
- Gruhler, C.; De Rosnay, P.; Hasenauer, S.; Holmes, T.; De Jeu, R.; Kerr, Y.; Mougin, E.; Njoku, E.; Timouk, F.; Wagner, W.; et al. Soil moisture active and passive microwave products: Intercomparison and evaluation over a Sahelian site. *Hydrol. Earth Syst. Sci.* **2010**, *14*, 141–156. [[CrossRef](#)]

10. Louvet, S.; Pellarin, T.; al Bitar, A.; Cappelaere, B.; Galle, S.; Grippa, M.; Gruhier, C.; Kerr, Y.; Lebel, T.; Mialon, A.; et al. SMOS soil moisture product evaluation over West-Africa from local to regional scale. *Remote Sens. Environ.* **2015**, *156*, 383–394. [[CrossRef](#)]
11. Frison, P.L.; Mougin, E.; Hiernaux, P. Observations and Interpretation of Seasonal ERS-1 Wind Scatterometer Data over Northern Sahel (Mali). *Remote Sens. Environ.* **1998**, *63*, 233–242. [[CrossRef](#)]
12. Frison, P.-L.; Jarlan, L.; Mougin, E. Using Satellite Scatterometers to Monitor Continental Surfaces. In *Land Surface Remote Sensing in Continental Hydrology*; Elsevier: New York, NY, USA, 2016; pp. 79–113, ISBN 9781785481048.
13. De Jeu, R.A.M.; Wagner, W.; Holmes, T.R.H.; Dolman, A.J.; van de Giesen, N.C.; Friesen, J. Global Soil Moisture Patterns Observed by Space Borne Microwave Radiometers and Scatterometers. *Surv. Geophys.* **2008**, *29*, 399–420. [[CrossRef](#)]
14. Naeimi, V.; Scipal, K.; Bartalis, Z.; Hasenauer, S.; Wagner, W. An Improved Soil Moisture Retrieval Algorithm for ERS and METOP Scatterometer Observations. *IEEE Trans. Geosci. Remote Sens.* **2009**, *47*, 1999–2013. [[CrossRef](#)]
15. Holgate, C.M.; De Jeu, R.A.M.; van Dijk, A.I.J.M.; Liu, Y.Y.; Renzullo, L.J.; Vinodkumar; Dharssi, I.; Parinussa, R.M.; Van Der Schalie, R.; Gevaert, A.; et al. Comparison of remotely sensed and modelled soil moisture data sets across Australia. *Remote Sens. Environ.* **2016**, *186*, 479–500. [[CrossRef](#)]
16. Tansey, K.J.; Millington, A.C.; Battikhi, A.M.; White, K.H. Monitoring soil moisture dynamics using satellite imaging radar in northeastern Jordan. *Appl. Geogr.* **1999**, *19*, 325–344. [[CrossRef](#)]
17. Moran, M.S.; Hymer, D.C.; Qi, J.; Sano, E.E. Soil moisture evaluation using multi-temporal synthetic aperture radar (SAR) in semiarid rangeland. *Agric. For. Meteorol.* **2000**, *105*, 69–80. [[CrossRef](#)]
18. Baup, F.; Mougin, E.; Hiernaux, P.; Lopes, A.; De Rosnay, P.; Chenerie, I. Radar Signatures of Sahelian Surfaces in Mali Using ENVISAT-ASAR Data. *IEEE Trans. Geosci. Remote Sens.* **2007**, *45*, 2354–2363. [[CrossRef](#)]
19. Baup, F.; Mougin, E.; De Rosnay, P.; Hiernaux, P.; Frappart, F.; Frison, P.L.; Zribi, M.; Viarre, J. Mapping surface soil moisture over the Gourma mesoscale site (Mali) by using ENVISAT ASAR data. *Hydrol. Earth Syst. Sci.* **2011**, *15*. [[CrossRef](#)]
20. Ridley, J.; Strawbridge, F.; Card, R.; Phillips, H. Radar backscatter characteristics of a desert surface. *Remote Sens. Environ.* **1996**, *57*, 63–78. [[CrossRef](#)]
21. Fatras, C.; Frappart, F.; Mougin, E.; Grippa, M.; Hiernaux, P. Estimating surface soil moisture over Sahel using ENVISAT radar altimetry. *Remote Sens. Environ.* **2012**, *123*. [[CrossRef](#)]
22. Fatras, C.; Frappart, F.; Mougin, E.; Frison, P.-L.; Faye, G.; Borderies, P.; Jarlan, L. Spaceborne altimetry and scatterometry backscattering signatures at C- and Ku-bands over West Africa. *Remote Sens. Environ.* **2015**, *159*. [[CrossRef](#)]
23. Frappart, F.; Fatras, C.; Mougin, E.; Marieu, V.; Diepkilé, A.T.; Blarel, F.; Borderies, P. Radar altimetry backscattering signatures at Ka, Ku, C, and S bands over West Africa. *Phys. Chem. Earth* **2015**, *83–84*. [[CrossRef](#)]
24. Bonnefond, P.; Verron, J.; Aublanc, J.; Babu, K.; Bergé-Nguyen, M.; Cancet, M.; Chaudhary, A.; Crétaux, J.-F.; Frappart, F.; Haines, B.; et al. The Benefits of the Ka-Band as Evidenced from the SARAL/AltiKa Altimetric Mission: Quality Assessment and Unique Characteristics of AltiKa Data. *Remote Sens.* **2018**, *10*, 83. [[CrossRef](#)]
25. Uebbing, B.; Forootan, E.; Braakmann-Folgmann, A.; Kusche, J. Inverting surface soil moisture information from satellite altimetry over arid and semi-arid regions. *Remote Sens. Environ.* **2017**, *196*, 205–223. [[CrossRef](#)]
26. Fatras, C.; Borderies, P.; Baghdadi, N.; Zribi, M.; El Hajj, M.; Frappart, F.; Mougin, E. Radar Backscattering Coefficient over Bare Soils at Ka-Band Close to Nadir Angle. *IEEE Geosci. Remote Sens. Lett.* **2016**, *13*, 1290–1294. [[CrossRef](#)]
27. Hallikainen, M.; Ulaby, F.; Dobson, M.; El-Rayes, M.; Wu, L. Microwave Dielectric Behavior of Wet Soil-Part 1: Empirical Models and Experimental Observations. *IEEE Trans. Geosci. Remote Sens.* **1985**, *23*, 25–34. [[CrossRef](#)]
28. Dobson, M.; Ulaby, F.; Hallikainen, M.; El-rayes, M. Microwave Dielectric Behavior of Wet Soil-Part II: Dielectric Mixing Models. *IEEE Trans. Geosci. Remote Sens.* **1985**, *23*, 35–46. [[CrossRef](#)]
29. Malmberg, C.G.; Maryott, A.A. Dielectric constant of water from 0 to 1000 °C. *J. Res. Natl. Bur. Stand.* **1956**, *56*, 1–8. [[CrossRef](#)]
30. Nashashibi, A.; Ulaby, F.T.; Sarabandi, K. Measurement and modeling of the millimeter-wave backscatter response of soil surfaces. *IEEE Trans. Geosci. Remote Sens.* **1996**, *34*, 561–572. [[CrossRef](#)]
31. Ulaby, F.T. *Radar Polarimetry for Geoscience Applications*; Fawwaz, T., Elachi, C., Eds.; Artech House: Norwood, MA, USA, 1990; ISBN 0890064067.

32. Ruck, G.T.; Barrick, D.E.; Stuart, W.D.; Krichbaum, C.K. *Radar Cross Section Handbook*; Plenum Press: New York, NY, USA, 1970; Volume 1.
33. Chelton, D.B.; Ries, J.C.; Haines, B.J.; Fu, L.-L.; Callahan, P.S. Chapter 1 Satellite Altimetry. In *Satellite Altimetry and Earth Sciences: A Handbook of Techniques and Applications*; Elsevier: New York, NY, USA, 2001; Volume 69, 131p, ISBN 0074-6142.
34. Biancamaria, S.; Frappart, F.; Leleu, A.-S.; Marieu, V.; Blumstein, D.; Desjonquères, J.-D.; Boy, F.; Sottolichio, A.; Valle-Levinson, A. Satellite radar altimetry water elevations performance over a 200 m wide river: Evaluation over the Garonne River. *Adv. Space Res.* **2017**, *59*, 128–146. [[CrossRef](#)]
35. CTOH (Center for Topographic studies of the Ocean and Hydrosphere). Available online: <http://ctoh.legos.obs-mip.fr> (accessed on 9 April 2018).
36. Zelli, C. ENVISAT RA-2 advanced radar altimeter: Instrument design and pre-launch performance assessment review. *Acta Astronaut.* **1999**, *44*, 323–333. [[CrossRef](#)]
37. Tachikawa, T.; Hato, M.; Kaku, M.; Iwasaki, A. The characteristics of ASTER GDEM version 2. In Proceedings of the IEEE International Geoscience and Remote Sensing Symposium, Vancouver, BC, Canada, 24–29 July 2011. [[CrossRef](#)]
38. Steunou, N.; Desjonquères, J.D.; Picot, N.; Sengenès, P.; Noubel, J.; Poisson, J.C. AltiKa Altimeter: Instrument Description and In Flight Performance. *Mar. Geod.* **2015**, *38*, 22–42. [[CrossRef](#)]
39. Mougin, E.; Hiernaux, P.; Kergoat, L.; Grippa, M.; de Rosnay, P.; Timouk, F.; Le Dantec, V.; Demarez, V.; Lavenu, F.; Arjounin, M.; et al. The AMMA-CATCH Gourma observatory site in Mali: Relating climatic variations to changes in vegetation, surface hydrology, fluxes and natural resources. *J. Hydrol.* **2009**, *375*. [[CrossRef](#)]
40. Frappart, F.; Hiernaux, P.; Guichard, F.; Mougin, E.; Kergoat, L.; Arjounin, M.; Lavenu, F.; Koité, M.; Paturol, J.-E.; Lebel, T. Rainfall regime across the Sahel band in the Gourma region, Mali. *J. Hydrol.* **2009**, *375*, 128–142. [[CrossRef](#)]
41. Wingham, D.J.; Rapley, C.G.; Griffiths, H. New Techniques in Satellite Altimeter Tracking Systems. In Proceedings of the 1986 International Geoscience and Remote Sensing Symposium on Remote Sensing, Zurich, Switzerland, 8–11 September 1986; pp. 1339–1344.
42. Frappart, F.; Calmant, S.; Cauhopé, M.; Seyler, F.; Cazenave, A. Preliminary results of ENVISAT RA-2-derived water levels validation over the Amazon basin. *Remote Sens. Environ.* **2006**, *100*. [[CrossRef](#)]
43. Boisot, O.; Pioch, S.; Fatras, C.; Caulliez, G.; Bringer, A.; Borderies, P.; Lalaurie, J.-C.; Guérin, C.-A. Ka-band backscattering from water surface at small incidence: A wind-wave tank study. *J. Geophys. Res. Oceans* **2015**, *120*, 3261–3285. [[CrossRef](#)]



© 2018 by the authors. Licensee MDPI, Basel, Switzerland. This article is an open access article distributed under the terms and conditions of the Creative Commons Attribution (CC BY) license (<http://creativecommons.org/licenses/by/4.0/>).